Nano Research

ISSN 1998-0124 CN 11-5974/O4
https://doi.org/10.1007/s12274-022-4388-1

Research Article

Abnormal anti-oxidation behavior of hexagonal boron nitride grown on copper

Li Wang[1,2,§] (✉), Jiajie Qi[1,§], Shuai Zhang[3,§], Mingchao Ding[2], Wei Wei[4], Jinhuan Wang[1,5], Zhihong Zhang[1], Ruixi Qiao[6], Zhibin Zhang[1], Zehui Li[1], Kehai Liu[7], Ying Fu[7], Hao Hong[1], Can Liu[1], Muhong Wu[6], Wenlong Wang[2], Jun He[8], Yi Cui[4], Qunyang Li[3] (✉), Xuedong Bai[2,9] (✉), and Kaihui Liu[1,6] (✉)

[1] *State Key Laboratory for Mesoscopic Physics, Frontiers Science Center for Nano-optoelectronics, School of Physics, Peking University, Beijing 100871, China*
[2] *Beijing National Laboratory for Condensed Matter Physics, Institute of Physics, Chinese Academy of Sciences, Beijing 100190, China*
[3] *Department of Engineering Mechanics, State Key Laboratory of Tribology, Tsinghua University, Beijing 100084, China*
[4] *Vacuum Interconnected Nanotech Workstation, Suzhou Institute of Nano-Tech and Nano-Bionics, Chinese Academy of Sciences, Suzhou 215123, China*
[5] *School of Chemistry and Chemical Engineering, Beijing Institute of Technology, Beijing 100081, China*
[6] *International Centre for Quantum Materials, Collaborative Innovation Centre of Quantum Matter, Peking University, Beijing 100871, China*
[7] *Songshan Lake Materials Laboratory, Institute of Physics, Chinese Academy of Sciences, Guangdong 523808, China*
[8] *CAS Center for Excellence in Nanoscience, CAS Key Laboratory of Nanosystem and Hierarchical Fabrication, National Center for Nanoscience and Technology, Beijing 100190, China*
[9] *School of Physical Sciences, University of Chinese Academy of Sciences, Beijing 100049, China*
[§] *Li Wang, Jiajie Qi, and Shuai Zhang contributed equally to this work.*

Received: 20 December 2021 / **Revised:** 15 March 2022 / **Accepted:** 5 April 2022

ABSTRACT

Atomic-layered hexagonal boron nitride (hBN) is expected to be the best two-dimensional (2D) anti-oxidation layer on metals for its incomparable impermeability, insulativity, and stability, as well as the progressive bottom-up growth techniques to ensure fast coating on metal surface in large area. However, its real anti-oxidation ability in practice is found to be unsatisfactory and nonuniform, and the main obstacle to achieving ideal anti-oxidation performance lies in unclear anti-oxidation behavior at special interface between 2D hBN and three-dimensional (3D) metals. Herein, system of monolayer hBN grown on copper (Cu) foils with various lattice orientations was grown to investigate the anti-oxidation behavior of different interlayer configurations. By using structural characterizations together with analysis of topography, we surprisingly found that stronger interlayer coupling led to worse anti-oxidation performance owing to fast diffusion of O_2 through higher hBN corrugations generated at the commensurate hBN/Cu(111) configuration. In view of this, we developed the approach of cyclic reannealing that can effectively flatten corrugations and steps, and therefore improve the anti-oxidation performance to a great extent. This work provides a more in-depth understanding of anti-oxidation behavior of 2D materials grown on 3D metals, and a practical method to pave the way for its large-scale applications in future.

KEYWORDS

hexagonal boron nitride, anti-oxidation of metals, nanoscale corrugation, cyclic reannealing method

1 Introduction

Coating of the protective layer is the most common way to address the oxidation of metals nowadays [1, 2]. It is the long-term pursuit for a material of protective layer having the optimal impermeability, adaptability, stability, and extreme thickness to maintain the physical properties of protected metals. The rise of two-dimensional (2D) materials has provided an opportunity that one material possesses all these properties [3–5], and therein the hexagonal boron nitride (hBN) is considered to be the most promising candidate due to excellent thermal conductivity [6] and exclusive insulativity from wide bandgap near to 6 eV [7–9]. Recently, growth techniques of large-sized single-crystal hBN monolayer on metal substrates have been developed [10–14], showing the possibility of fast coating of high-quality hBN film on metal in large area. With all these superiorities, hBN is highly anticipated that can protect the metals with special structure in practice, such as copper interconnects in chips, or the copper cooling modules with designed structures, etc.

However, the real anti-oxidation ability of hBN is in controversial, as the anti-oxidation mechanism of hBN grown on metals is unclear [15–21]. Previously, intercalation of O_2 was reported in system of hBN/Cu(100) (hBN grown on Cu(100)), implying that diffusion of small molecules might be happened at the interface between 2D hBN and three-dimensional (3D) metals

Address correspondence to Li Wang, liwang@iphy.ac.cn; Qunyang Li, qunyang@tsinghua.edu.cn; Xuedong Bai, xdbai@iphy.ac.cn; Kaihui Liu, khliu@pku.edu.cn

[22]. Moreover, linear wrinkles in incommensurate graphene/Cu(100) were proved that can facilitate the diffusion of H_2O, and commensurate graphene/Cu(111) was found to be much flatter and therefore possess the much better anti-oxidation performance [23], indicating that the diffusion behavior at 2D/3D interface is correlated to interlayer configuration. Compared to graphene, the actual anti-oxidation ability of hBN is seriously inconsistent with the prediction by its excellent properties in theory, hence a more in-depth understanding of the anti-oxidation behavior of hBN grown on metals needs to be studied.

In this work, we grew the hBN domains on one piece of single-crystal Cu(111) with equal quality but various lattice orientations, to form the different interfacial configurations. The color contrast and the different peak intensities of Cu_2O Raman spectra after fixed baking test were employed to reveal the relative anti-oxidation performance with the dependence of interfacial configuration. An unexpected phenomenon that commensurate hBN/Cu(111) with the strongest interfacial coupling (and also the most energetically preferred during the epitaxial growth [24]) exhibited the worst anti-oxidation performance was clearly observed. The analysis of topography at joint area of commensurate and incommensurate hBN domains was carried out, and corrugations of hBN were found to be related to the diffusion of O_2 at the interface between hBN and Cu(111). In consequence, we developed an approach of cyclic reannealing, and proved that can effectively flatten the corrugations of hBN domains no matter what lattice orientation, and bunched steps on Cu surface as well, then greatly promote the anti-oxidation performance of hBN/Cu(111) over all. Our research not only discovered an abnormal anti-oxidation behavior caused by corrugations, but also provided a universal method for reaching the nearly perfect anti-oxidation performance of monolayer hBN grown on metals.

2 Results and discussion

2.1 Anti-oxidation performance of hBN/Cu(111) with different grain orientations

In our experiments, hBN/Cu(111) with aligned and unaligned orientations was baked in dry air immediately after growth to accelerate the oxidation process and preclude the influence of water. *In-situ* optical images were taken at the moments with identical time interval and with the same parameters to estimate the degree of oxidation through the color evolution, because the wavelength of reflected light from oxidized hBN/Cu(111) was correlated to the thickness of as-synthesized Cu_2O (Fig. S1(a) in the Electronic Supplementary Material (ESM)) at interface [25]. It was natural that the oxidation of bare Cu was faster, but it was unexpected that the anti-oxidation ability of aligned hBN domains was apparently worse than that of unaligned hBN domains (Figs. 1(a)–1(c)). The sharp peak of Cu(111) in X-ray diffraction (XRD) spectrum measured after baking test indicated just very thin layer of Cu_2O synthesized on surface of Cu foil (Fig. 1(d)), so Raman spectra measurement could be employed to reconfirm the oxidation degree here (Fig. 1(e)), for higher intensity of Cu_2O Raman peaks reflecting thicker Cu_2O layer when size of beam spot was fixed (Fig. S1(b) in the ESM) [26, 27]. Moreover, the hBN domains after baking test were also transferred onto SiO_2/Si wafer or transmission electron microscopy (TEM) grid to corroborate the uniform monolayer and intact lattice by X-ray photoelectron spectroscopy (XPS) (Fig. 1(f)), Raman spectroscopy (Fig. S2(a) in the ESM), the second harmonic generation (SHG) mapping (Fig. S2(b) in the ESM), atomic force microscopy (AFM) scan (Fig. S2(c) in the ESM), as well as the atomically resolved scanning transmission electron microscopy (STEM) image (inset of Fig. 1(f)).

2.2 Characterizations of interfacial configuration of hBN/Cu(111)

Interfacial configuration of hBN/Cu(111) was determined by the photoemission electron microscopy (PEEM) combined with low-energy electron diffraction (LEED). Typical area including both aligned and unaligned hBN domains was located in PEEM image (Fig. 2(a)), then LEED patterns were collected in corresponding area to reveal their reciprocal lattices in detail (Figs. 2(b) and 2(c)). As the lattices of hBN and Cu(111) are of the same symmetry and the very close lattice constant, a set of diffraction patterns with the same orientation collected at aligned hBN domains grown on

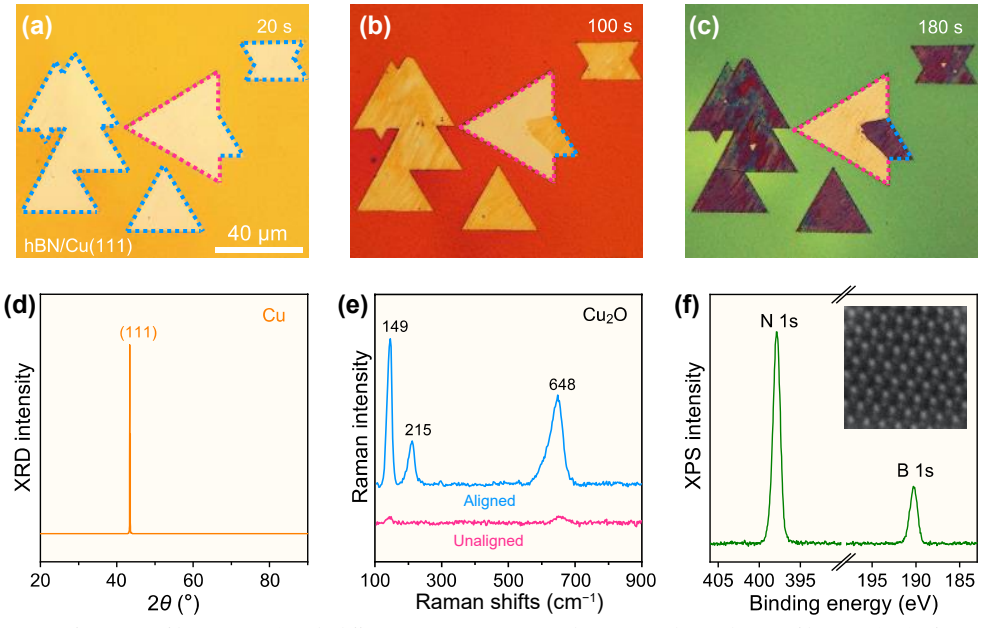

Figure 1 Anti-oxidation performance of hBN/Cu(111) with different grain orientations. The *in-situ* color evolution of hBN/Cu(111) after oxidation in the drying oven at 220 °C for (a) 20 s, (b) 100 s, and (c) 180 s, respectively. Aligned and unaligned hBN domains are marked with blue and red dotted lines, respectively. (d) XRD spectrum of 2θ scanning of Cu(111) and (e) Raman spectra of Cu_2O collected at aligned and unaligned hBN/Cu(111) after baking test. (f) XPS spectra and atomically resolved STEM image (inset) of hBN after baking test.

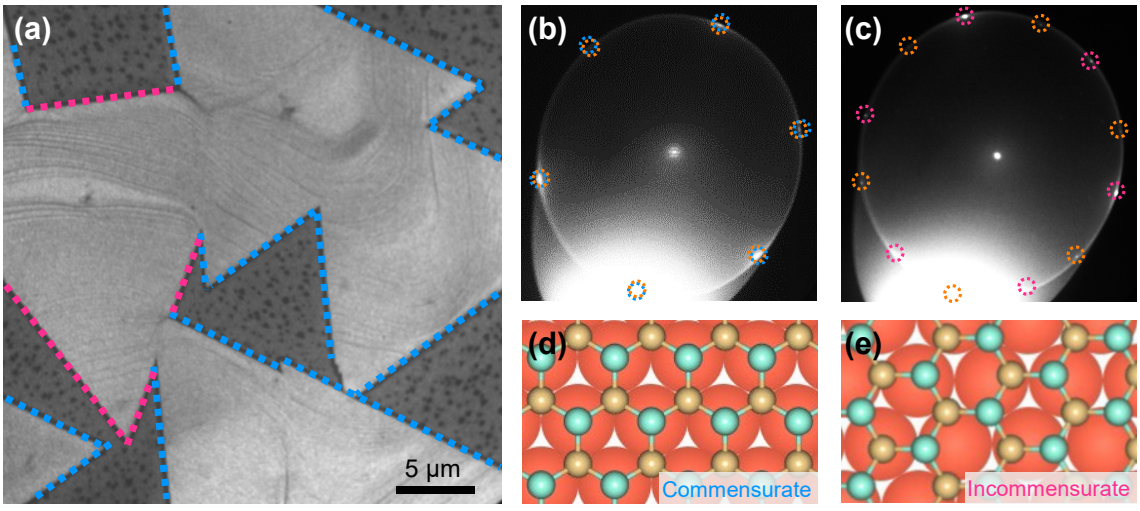

Figure 2 Characterizations of interfacial configuration of hBN/Cu(111). (a) PEEM image of a typical area including both aligned and unaligned hBN domains. LEED patterns of (b) aligned (blue dotted circles) and (c) unaligned (red dotted circles) hBN domain on Cu(111) (orange dotted circles). Schematic diagrams showing that (d) aligned and (e) unaligned hBN lattice on Cu(111) are of the commensurate and incommensurate configuration, respectively.

Cu(111) indicated the commensurate configuration of hBN/Cu(111) (Fig. 2(d)) [28, 29]. On the contrary, unaligned hBN domains on Cu(111) had incommensurate interfacial configuration (Fig. 2(e)).

2.3 Interfacial configuration dependent anti-oxidation behavior of hBN/Cu(111)

Commensurate configuration was known for the strongest interlayer coupling, which was expected to have the best anti-oxidation performance for the least chance to form wrinkles [23, 24, 30]. Hence, worse anti-oxidation performance found in commensurate hBN/Cu(111) should not be originated from linear wrinkles commonly seen in 2D materials. Atomic steps of Cu(111) were observed that can bunch together and turn into the "high steps" after growth of hBN, then provide channels to facilitate the leakage and diffusion of oxygen at interface. We mapped the topography of hBN/Cu(111) through AFM scanning and found that those steps were of similar height and density in regions of commensurate and incommensurate hBN/Cu(111) (Figs. S3(a)–S3(c) in the ESM), indicating that the inconsistent anti-oxidation performance did not come from bunched steps as well. However, at step surface, the significant difference of roughness and height distribution in commensurate and incommensurate regions was shown from the highly resolved height map (Figs. 3(a) and 3(b)). It was reported that the corrugations would be formed in hBN grown on metals with face-centered cubic (FCC) (111) facet [31–35], thereby much higher corrugations were found in commensurate hBN/Cu(111) (schematically illustrated in Fig. 3(c)). Considering the pre-existing space about 0.3 nm between hBN and Cu(111) [35], which is basically the same size as O_2 molecule [36], higher corrugations undoubtedly led to fast diffusion of more O_2 molecules at interface, and therefore degraded the anti-oxidation performance to the great extent (schematically illustrated in Fig. 3(d)).

Moreover, we specially grew more incommensurate hBN domains on same single-crystal Cu(111) with different rotation angles (γ is defined to be the rotation angle between a hBN domain and the commensurate hBN domain), and carried out the AFM scan right after growth (Figs. S4(a)–S4(e) in the ESM) as well as the subsequent oxidation test in dry air (Figs. S4(f)–S4(h) in the ESM). The intensities of Cu_2O Raman peaks (lower panel in Fig. 3(e)) and the average roughness were also collected in AFM maps (upper panel in Fig. 3(e)) with dependence of rotation angle were plotted (see details in the Methods Section), respectively. Two curves with a similar downtrend here clearly stated that stronger interlayer coupling (of lower γ) between hBN and Cu(111) would lead to weaker anti-oxidation performance due to higher corrugations of hBN. It was reported that corrugations of hBN on FCC(111) facet of metals were attributed to orbital overlap between d states of transition metals and π states of hBN [33], thus stronger binding in smaller interlayer spacing would generate more strain to form higher corrugations of hBN after growth, in view of significantly different coefficients of thermal expansion in hBN and metals.

2.4 Improving anti-oxidation performance of hBN/Cu(111) through cyclic reannealing

As commensurate hBN/Cu(111) is the most energetically preferred orientation in epitaxial growth, high corrugations would severely hinder the practical anti-oxidation applications of hBN. To solve this problem, we have developed a method of cyclic reannealing after growth (diagram of procedure shown in Fig. S5(a) in the ESM) to flatten the corrugations by releasing the strain [37, 38]. A comparative experiment (see details in the Experimental Section, and diagram of procedure in Fig. S5(b) in the ESM) was also carried out, to prove that flattening of steps and corrugations is related to the times of reannealing, instead of the reannealing time in total, by comparing anti-oxidation performances shown in Fig. 4(c) and Fig. S5(c) in the ESM. Through the repeated warming and cooling process, we found that the bunched steps were flattened (Figs. S6(a)–S6(c) in the ESM), height of corrugations was reduced, and discrepancy of height in commensurate and incommensurate region was eliminated (Figs. 4(a) and 4(b)). Accordingly, anti-oxidation ability of commensurate and incommensurate hBN domains were enhanced and equalized as well (Figs. S7(a) and S7(b) in the ESM and Fig. 4(c)). With increasing times of reannealing, intensity of Cu_2O Raman peaks (lower panel in Fig. 4(d)) and average roughness (upper panel in Fig. 4(d)) for both commensurate and incommensurate hBN/Cu(111) showed the similar downtrend, confirming the anti-oxidation behavior driven by steps and corrugations. Besides, we noticed the enhancement of anti-oxidation performance almost reaching to the limit after 4-times reannealing, since the curve of Raman intensity of Cu_2O layer no longer exhibited the clear downtrend at this point (lower panel in Fig. 4(d)).

In addition, continuous hBN films with commensurate and incommensurate domains were grown on Cu(111), and its anti-

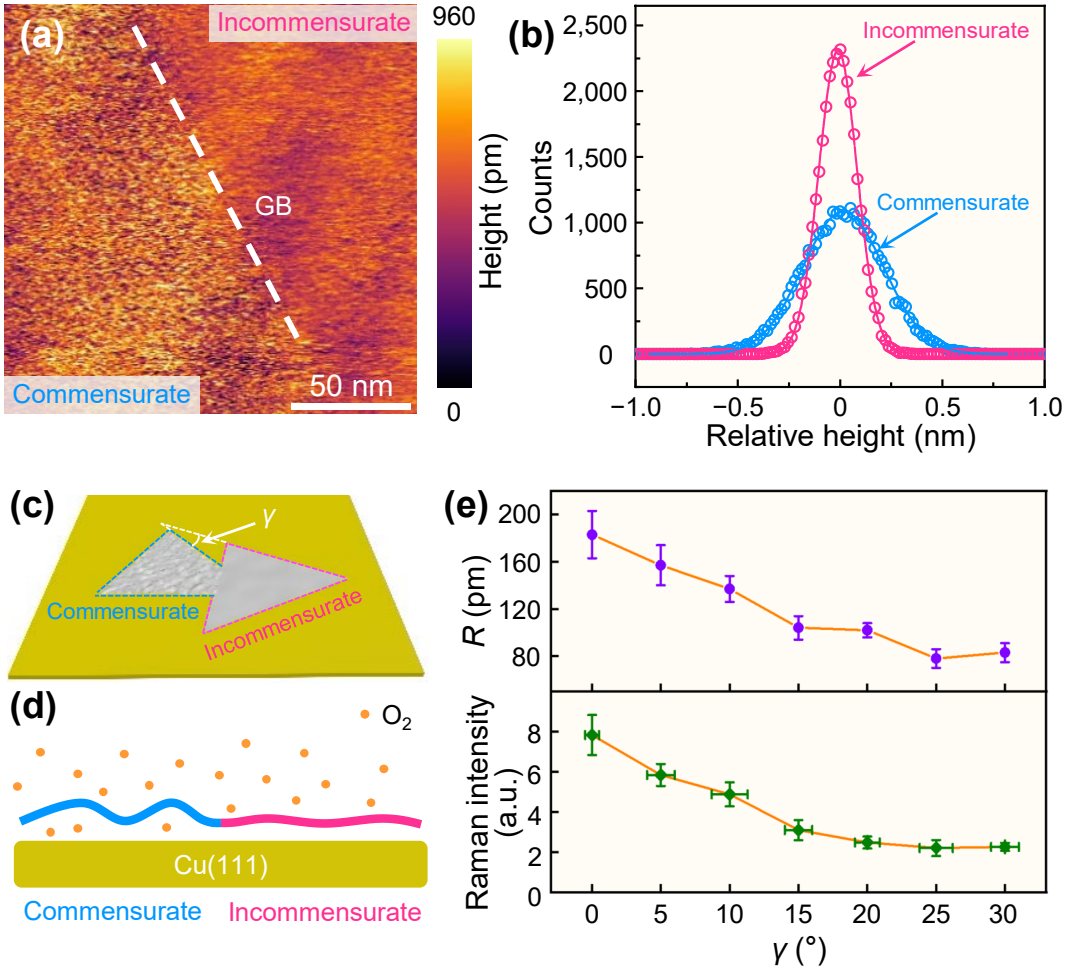

Figure 3 Interfacial configuration dependent anti-oxidation behavior of hBN/Cu(111). (a) AFM height map at the region around grain boundary between commensurate and incommensurate hBN/Cu(111) right after growth, of which the average roughness is 182 and 83 pm, respectively. (b) Relative height distribution collected in the area of commensurate and incommensurate hBN/Cu(111) shown in (a). (c) Schematic illustration of the corrugations in commensurate and incommensurate hBN domain grown on Cu(111), and γ is defined to be the rotation angle between a hBN domain and the commensurate hBN domain. (d) Schematic illustration of fast diffusion of O_2 in commensurate hBN/Cu(111) from side view. (e) Plots of rotation-angle-dependent average roughness (R) collected from AFM height map (upper panel) and intensity of Cu_2O Raman peaks (lower panel). The vertical and horizontal error bars represent the standard errors in data collection and observation errors of rotation angles (γ).

oxidation ability was found to be unsatisfactory and inconsistent (Figs. S8(a) and S8(b) in the ESM). After 4-times reannealing, anti-oxidation ability of entire hBN film was greatly enhanced, and the difference in anti-oxidation ability was also eliminated (Figs. S8(c) and S8(d) in the ESM). This was of same scenario of isolate hBN domains displayed previously (Figs. 1(c) and 4(c)), indicating that continuous film and isolate domains of hBN grown on Cu(111) shared the same anti-oxidation behavior. As a comparison, we also evaluated the improvement of anti-oxidation performance of single-crystal hBN films grown on Cu(111) with the size greater than 1 cm × 1 cm, and found that 4-time reannealing could also promote the anti-oxidation ability of large-area hBN film with fully commensurate interlayer configuration from the worst to near-perfect level (Fig. S9 in the ESM). With these anti-oxidation examinations at different scales, excellent effectiveness and broad practicability of cyclic reannealing could be well substantiated.

3 Conclusion

In summary, abnormal anti-oxidation behavior of hBN/Cu(111) was fully studied. It was shown that stronger interlayer coupling between hBN and Cu(111) led to weaker anti-oxidation performance due to the higher corrugations of hBN. To release the strain and flatten the corrugations and steps, the approach of cyclic reannealing was developed and proved that can promote the anti-oxidation performance of large-area hBN/Cu(111) to near perfectness. The findings in this work not only deepened the understanding about the anti-oxidation behavior, but also advanced the anti-oxidation technology of 2D materials grown on metals.

4 Experimental section

Growth of hBN domains with different orientations on single-crystal Cu(111): A polycrystalline Cu foil (25 μm thick, 99.8%; Sichuan Oriental Stars Trading Co. Ltd) was loaded into a quartz tube (diameter 6 cm and length 2 m) at the place of the heating zone (length 50 cm) of tube furnace, and ammonia borane (97%; Aldrich) was filled into an Al_2O_3 crucible and placed at upstream 1 m away from the Cu foil substrate. The substrate was heated to 1,050 °C in 1 h with mixed gas flow of Ar (500 sccm) and H_2 (50 sccm) at atmospheric pressure, followed by annealing with the same gas flow for 1 h to obtain single-crystal Cu(111). Afterward, the system was switched to low pressure (about 200 Pa) with mixed gas flow of Ar (10 sccm) and H_2 (40 sccm), while the ammonia borane was heated to 65 °C (95 °C for specially growing more incommensurate hBN domains with diverse orientations) within 10 min and kept at 65 °C for 1.5 h via a belt heater wrapped around the tube to sublimate ammonia borane and grow hBN. After growth, the whole chemical vapor deposition (CVD) system

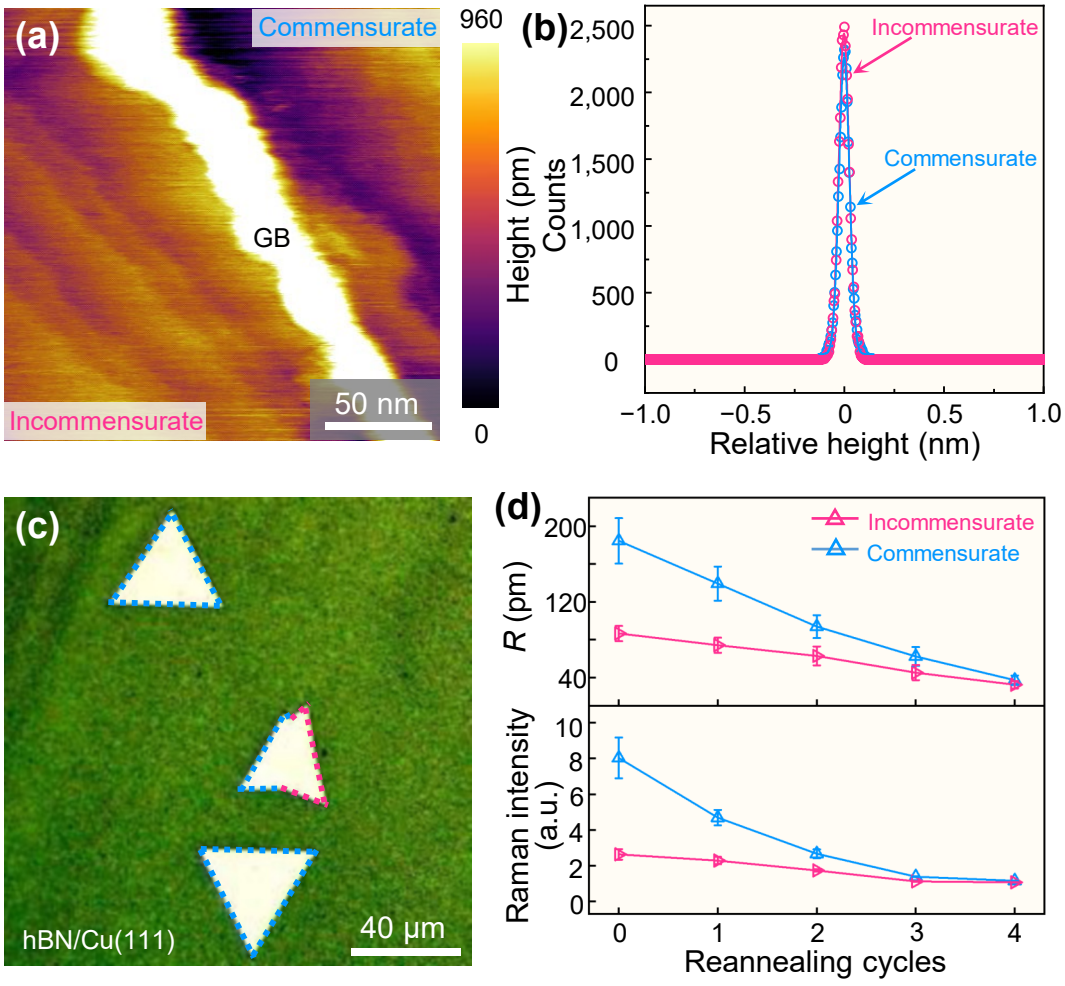

Figure 4 Improving anti-oxidation performance of hBN/Cu(111) through cyclic reannealing. (a) AFM height map at the region around grain boundary between commensurate (right) and incommensurate (left) hBN/Cu(111) right after 4-time reannealing, of which the average roughness is 36 and 32 pm, respectively. (b) Relative height distributions collected in area of commensurate and incommensurate hBN/Cu(111) shown in (a). (c) Optical image of 4-time reannealed hBN/Cu(111) with commensurate and incommensurate interfacial configurations after oxidation test in dry air. (d) Plot of average roughness (upper panel) and intensity of Cu_2O Raman peaks (lower panel) with respect to times of reannealing for both commensurate and incommensurate hBN/Cu(111). The error bars represent the standard errors in data collection.

was naturally cooled to room temperature with the gas flow of Ar (500 sccm) and H_2 (10 sccm) at atmospheric pressure.

Baking test of as-grown hBN/Cu(111): Baking oven (Hefei Kejing Co. Ltd) was warmed up to 220 °C in advance. Then hBN/Cu(111) was placed at a fixed position in the chamber of baking oven and baked at 220 °C right after growth (or reannealing), with the relative humidity (RH) < 2%. Except the *in-situ* oxidation test shown in Figs. 1(a)–1(c), baking time was fixed to be 180 seconds and 10 min for single domains and continuous films, respectively.

Post thermal treatment of as-grown hBN/Cu(111): (1) Cyclic reannealing process: As-grown hBN/Cu(111) was cut into several pieces, then reannealed for different times right after growth. In each time, sample was reheated to 550 °C within 0.5 h, then reannealed at 550 °C for 2 h with mixed gas flow of Ar (500 sccm) and H_2 (50 sccm) at atmospheric pressure. Afterward, sample was naturally cooled down to room temperature in about 2.5 h (diagram of cyclic reannealing procedure is shown in Fig. S5(a) in the ESM). (2) Long-time reannealing process: Sample was reheated to 550 °C within 0.5 h, then reannealed at 550 °C for 8 h with mixed gas flow of Ar (500 sccm) and H_2 (50 sccm) at atmospheric pressure. Afterward, sample was naturally cooled down to room temperature in about 2.5 h (diagram of long-time annealing procedure shown in Fig. S5(b) in the ESM).

Transfer of hBN: The hBN/Cu(111) was firstly spin-coated with polymethyl methacrylate (PMMA) and baked at 130 °C for 3 min in air, then floating on the surface of ammonium persulphate solution for 6 h for etching of the Cu underlying. After rinse with deionized (DI) water for 3 times, the samples were placed onto various metal substrates (Alfa Aesar), holey-carbon-film TEM grids (Zhongjingkeyi GIG-1213-3C), or SiO_2/Si wafter (Hefei Kejing Co. Ltd). Afterward, the resident PMMA was removed by rinse with acetone.

Optical microscope photographing: Optical images were obtained using a microscope (Olympus BX51 microscope). The brightness of light source and the exposure time was fixed to be 30% and 24 ms, respectively, and the white balance was set to be: R:G:B = 1:1:1.

Raman spectra measurements: Raman spectra were performed at room temperature using a home-made system with a laser excitation wavelength of 532 nm and a fixed power of about 3 mW, and the integrating time was fixed to be 10 s. Each average intensities of Cu_2O Raman peak required the measurements of Raman spectra at randomly selected 5 positions for each domain on total of 10 domains. Raman peak at 648 cm^{-1} with strong signal was chosen to avoid the peak of low wave number Raman shift [26, 27].

XPS, XRD, SHG, SEM, STEM, PEEM, and LEED measurements: XPS was performed using axis ultra imaging X-ray photoelectron spectrometer. XRD 2θ scan measurements were

conducted using a Bruker D8 Advance system with a copper target whose wavelength was ~ 1.54 Å. SHG mapping was collected by WiTec UHTS300 with incident light wavelength of 1,064 nm and a fixed excitation power of 20 mW. SEM and STEM images were obtained using a FEI Nova NanoSEM 430 scanning electron microscope and a Nion UltraSTEM 200 instrument operated at 60 kV, respectively. PEEM imaging experiments were performed in a SPECS PEEM system consisting of a preparation chamber and a main chamber (base pressure < 3×10^{-10} mbar). In this instrument, μ-LEED mode can be performed to investigate the surface structure from local regions.

AFM measurement: Asylum research cypher AFM was employed to perform topography measurements in ambient conditions (about 25 °C) under contact mode with the silicon nitride probes (Budget Sensors, SiNi) and conductive probes (Asylum Research, ASYELEC-01), respectively. Each average roughness required the measurements at randomly selected 5 regions (area of 5,000 nm^2 for each region) in the typical hBN domain with specific orientation (or times of reannealing) on Cu(111) immediately after growth (or reannealing).

Acknowledgements

L. W., J. J. Q., and S. Z. contributed equally to this work. This work was supported by the Guangdong Major Project of Basic and Applied Basic Research (2021B0301030002), the National Natural Science Foundation of China (Nos. 52025023, 51991342, 52021006, 11888101, 12025203, and 12104493), the Key Research & Development Program of Guangdong Province (Nos. 2020B010189001, 2019B010931001, and 2018B030327001), the Strategic Priority Research Program of Chinese Academy of Sciences (Nos. XDB33000000 and XDB33030200), Beijing Natural Science Foundation (No. JQ19004), Natural Science Foundation of Jiangsu Province (No. BK20170426), the Initiative Program of State Key Laboratory of Tribology (No. SKLT2019B02), National Key R&D Program of China (No. 2018YFA0703700), Program from Chinese Academy of Sciences (No. E0K5231B11), and the Pearl River Talent Recruitment Program of Guangdong Province (No. 2019ZT08C321). The authors are grateful for the support from the Electron Microscopy Laboratory in Peking University for the use of electron microscope, and the Vacuum Interconnected Nanotech Workstation (NANO-X) of Suzhou Institute of Nano-Tech and Nano-Bionics, the Chinese Academy of Sciences.

Electronic Supplementary Material: Supplementary material (additional optical images, Raman, SHG and AFM characterizations) is available in the online version of this article at https://doi.org/10.1007/s12274-022-4388-1.

References

[1] Pryor, M. J. Cathodic protection of iron. *Nature* **1956**, *178*, 1245–1246.

[2] Su, Y.; Kravets, V. G.; Wong, S. L.; Waters, J.; Geim, A. K.; Nair, R. R. Impermeable barrier films and protective coatings based on reduced graphene oxide. *Nat. Commun.* **2014**, *5*, 4843.

[3] Geim, A. K.; Novoselov, K. S. The rise of graphene. *Nat. Mater.* **2007**, *6*, 183–191.

[4] Dean, C. R.; Young, A. F.; Meric, I.; Lee, C.; Wang, L.; Sorgenfrei, S.; Watanabe, K.; Taniguchi, T.; Kim, P.; Shepard, K. L. et al. Boron nitride substrates for high-quality graphene electronics. *Nat. Nanotechnol.* **2010**, *5*, 722–726.

[5] Hu, S.; Lozada-Hidalgo, M.; Wang, F. C.; Mishchenko, A.; Schedin, F.; Nair, R. R.; Hill, E. W.; Boukhvalov, D. W.; Katsnelson, M. I.; Dryfe, R. A. W. et al. Proton transport through one-atom-thick crystals. *Nature* **2014**, *516*, 227–230.

[6] Cai, Q. R.; Scullion, D.; Gan, W.; Falin, A.; Zhang, S. Y.; Watanabe, K.; Taniguchi, T.; Chen, Y.; Santos, E. J. G.; Li, L. H. High thermal conductivity of high-quality monolayer boron nitride and its thermal expansion. *Sci. Adv.* **2019**, *5*, eaav0129.

[7] Kubota, Y.; Watanabe, K.; Tsuda, O.; Taniguchi, T. Deep ultraviolet light-emitting hexagonal boron nitride synthesized at atmospheric pressure. *Science* **2007**, *317*, 932–934.

[8] Cassabois, G.; Valvin, P.; Gil, B. Hexagonal boron nitride is an indirect bandgap semiconductor. *Nat. Photonics* **2016**, *10*, 262–266.

[9] Li, L. H.; Chen, Y. Atomically thin boron nitride: Unique properties and applications. *Adv. Funct. Mater.* **2016**, *26*, 2594–2608.

[10] Lu, G. Y.; Wu, T. R.; Yuan, Q. H.; Wang, H. S.; Wang, H. M.; Ding, F.; Xie, X. M.; Jiang, M. H. Synthesis of large single-crystal hexagonal boron nitride grains on Cu-Ni alloy. *Nat. Commun.* **2015**, *6*, 6160.

[11] Lee, J. S.; Choi, S. H.; Yun, S. J.; Kim, Y. I.; Boandoh, S.; Park, J. H.; Shin, B. G.; Ko, H.; Lee, S. H.; Kim, Y. M. et al. Wafer-scale single-crystal hexagonal boron nitride film via self-collimated grain formation. *Science* **2018**, *362*, 817–821.

[12] Wang, L.; Xu, X. Z.; Zhang, L. N.; Qiao, R. X.; Wu, M. H.; Wang, Z. C.; Zhang, S.; Liang, J.; Zhang, Z. H.; Zhang, Z. B. et al. Epitaxial growth of a 100-square-centimetre single-crystal hexagonal boron nitride monolayer on copper. *Nature* **2019**, *570*, 91–95.

[13] Chen, T. A.; Chuu, C. P.; Tseng, C. C.; Wen, C. K.; Wong, H. S. P.; Pan, S. Y.; Li, R. T.; Chao, T. A.; Chueh, W. C.; Zhang, Y. F. et al. Wafer-scale single-crystal hexagonal boron nitride monolayers on Cu (111). *Nature* **2020**, *579*, 219–223.

[14] Liu, C.; Wang, L.; Qi, J. J.; Liu, K. H. Designed growth of large-size 2D single crystals. *Adv. Mater.* **2020**, *32*, 2000046.

[15] Husain, E.; Narayanan, T. N.; Taha-Tijerina, J. J.; Vinod, S.; Vajtai, R.; Ajayan, P. M. Marine corrosion protective coatings of hexagonal boron nitride thin films on stainless steel. *ACS Appl. Mater. Interfaces* **2013**, *5*, 4129–4135.

[16] Liu, Z.; Gong, Y. J.; Zhou, W.; Ma, L. L.; Yu, J. J.; Idrobo, J. C.; Jung, J.; MacDonald, A. H.; Vajtai, R.; Lou, J. et al. Ultrathin high-temperature oxidation-resistant coatings of hexagonal boron nitride. *Nat. Commun.* **2013**, *4*, 2541.

[17] Jiang, L. L.; Xiao, N.; Wang, B. R.; Grustan-Gutierrez, E.; Jing, X.; Babor, P.; Kolíbal, M.; Lu, G. Y.; Wu, T. R.; Wang, H. M. et al. High-resolution characterization of hexagonal boron nitride coatings exposed to aqueous and air oxidative environments. *Nano Res.* **2017**, *10*, 2046–2055.

[18] Khan, M. H.; Jamali, S. S.; Lyalin, A.; Molino, P. J.; Jiang, L.; Liu, H. K.; Taketsugu, T.; Huang, Z. G. Atomically thin hexagonal boron nitride nanofilm for Cu protection: The importance of film perfection. *Adv. Mater.* **2017**, *29*, 1603937.

[19] Chilkoor, G.; Karanam, S. P.; Star, S.; Shrestha, N.; Sani, R. K.; Upadhyayula, V. K. K.; Ghoshal, D.; Koratkar, N. A.; Meyyappan, M.; Gadhamshetty, V. Hexagonal boron nitride: The thinnest insulating barrier to microbial corrosion. *ACS Nano* **2018**, *12*, 2242–2252.

[20] Chilkoor, G.; Jawaharraj, K.; Vemuri, B.; Kutana, A.; Tripathi, M.; Kota, D.; Arif, T.; Filleter, T.; Dalton, A. B.; Yakobson, B. I. et al. Hexagonal boron nitride for sulfur corrosion inhibition. *ACS Nano* **2020**, *14*, 14809–14819.

[21] Liu, G. Z.; Wang, J.; Ge, Y. H.; Wang, Y. J.; Lu, S. Q.; Zhao, Y.; Tang, Y.; Soomro, A. M.; Hong, Q. M.; Yang, X. D. et al. Cu nanowires passivated with hexagonal boron nitride: An ultrastable, selectively transparent conductor. *ACS Nano* **2020**, *14*, 6761–6773.

[22] Ma, C. X.; Park, J.; Liu, L.; Kim, Y. S.; Yoon, M.; Baddorf, A. P.; Gu, G.; Li, A. P. Interplay between intercalated oxygen superstructures and monolayer h-BN on Cu(100). *Phys. Rev. B* **2016**, *94*, 064106.

[23] Xu, X. Z.; Yi, D.; Wang, Z. C.; Yu, J. C.; Zhang, Z. H.; Qiao, R. X.; Sun, Z. H.; Hu, Z. H.; Gao, P.; Peng, H. L. et al. Greatly enhanced anticorrosion of Cu by commensurate graphene coating. *Adv. Mater.* **2018**, *30*, 1702944.

[24] Li, J. D.; Li, Y.; Yin, J.; Ren, X. B.; Liu, X. F.; Jin, C. H.; Guo, W. L. Growth of polar hexagonal boron nitride monolayer on nonpolar copper with unique orientation. *Small* **2016**, *12*, 3645–3650.

[25] Zhang, Z. B.; Xu, X. Z.; Zhang, Z. H.; Wu, M. H.; Wang, J. H.; Liu, C.; Shang, N. Z.; Wang, J. X.; Gao, P.; Yu, D. P. et al. Identification of copper surface index by optical contrast. *Adv. Mater. Interfaces* **2018**, *5*, 1800377.

[26] Yin, X. L.; Li, Y. L.; Ke, F.; Lin, C. F.; Zhao, H. B.; Gan, L.; Luo, Z. T.; Zhao, R. G.; Heinz, T. F.; Hu, Z. H. Evolution of the Raman spectrum of graphene grown on copper upon oxidation of the substrate. *Nano Res.* **2014**, *7*, 1613–1622.

[27] Galbiati, M.; Stoot, A. C.; Mackenzie, D. M. A.; Bøggild, P.; Camilli, L. Real-time oxide evolution of copper protected by graphene and boron nitride barriers. *Sci. Rep.* **2017**, *7*, 39770.

[28] Roth, S.; Matsui, F.; Greber, T.; Osterwalder, J. Chemical vapor deposition and characterization of aligned and incommensurate graphene/hexagonal boron nitride heterostack on Cu(111). *Nano Lett.* **2013**, *13*, 2668–2675.

[29] Shin, H. C.; Jang, Y.; Kim, T. H.; Lee, J. H.; Oh, D. H.; Ahn, S. J.; Lee, J. H.; Moon, Y.; Park, J. H.; Yoo, S. J. et al. Epitaxial growth of a single-crystal hybridized boron nitride and graphene layer on a wide-band gap semiconductor. *J. Am. Chem. Soc.* **2015**, *137*, 6897–6905.

[30] Woods, C. R.; Britnell, L.; Eckmann, A.; Ma, R. S.; Lu, J. C.; Guo, H. M.; Lin, X.; Yu, G. L.; Cao, Y.; Gorbachev, R. V. et al. Commensurate-incommensurate transition in graphene on hexagonal boron nitride. *Nat. Phys.* **2014**, *10*, 451–456.

[31] Corso, M.; Auwärter, W.; Muntwiler, M.; Tamai, A.; Greber, T.; Osterwalder, J. Boron nitride nanomesh. *Science* **2004**, *303*, 217–220.

[32] Laskowski, R.; Blaha, P.; Gallauner, T.; Schwarz, K. Single-layer model of the hexagonal boron nitride nanomesh on the Rh(111) surface. *Phys. Rev. Lett.* **2007**, *98*, 106802.

[33] Preobrajenski, A. B.; Vinogradov, A. S.; Ng, M. L.; Ćavar, E.; Westerström, R.; Mikkelsen, A.; Lundgren, E.; Mårtensson, N. Influence of chemical interaction at the lattice-mismatched h-BN/Rh(111) and h-BN/Pt(111) interfaces on the overlayer morphology. *Phys. Rev. B* **2007**, *75*, 245412.

[34] Joshi, S.; Ecija, D.; Koitz, R.; Iannuzzi, M.; Seitsonen, A. P.; Hutter, J.; Sachdev, H.; Vijayaraghavan, S.; Bischoff, F.; Seufert, K. et al. Boron nitride on Cu(111): An electronically corrugated monolayer. *Nano Lett.* **2012**, *12*, 5821–5828.

[35] Schwarz, M.; Riss, A.; Garnica, M.; Ducke, J.; Deimel, P. S.; Duncan, D. A.; Thakur, P. K.; Lee, T. L.; Seitsonen, A. P.; Barth, J. V. et al. Corrugation in the weakly interacting hexagonal-BN/Cu(111) system: Structure determination by combining noncontact atomic force microscopy and X-ray standing waves. *ACS Nano* **2017**, *11*, 9151–9161.

[36] Vallejos-Burgos, F.; Coudert, F. X.; Kaneko, K. Air separation with graphene mediated by nanowindow-rim concerted motion. *Nat. Commun.* **2018**, *9*, 1812.

[37] Lin, J. J.; Tay, R. Y.; Li, H. L.; Jing, L.; Tsang, S. H.; Wang, H.; Zhu, M. M.; McCulloch, D. G.; Teo, E. H. T. Smoothening of wrinkles in CVD-grown hexagonal boron nitride films. *Nanoscale* **2018**, *10*, 16243–16251.

[38] Yi, D.; Luo, D.; Wang, Z. J.; Dong, J. C.; Zhang, X.; Willinger, M. G.; Ruoff, R. S.; Ding, F. What drives metal-surface step bunching in graphene chemical vapor deposition. *Phys. Rev. Lett.* **2018**, *120*, 246101.